

February 27, 2026

SULFUR FRACTIONATION IN CORONAL PLUMES AS OBSERVED BY SOLAR ORBITER/SPICE

SLIMANE MZERGUAAT, MIHO JANVIER, ERIC BUCHLIN, DEBORAH BAKER, ANDY S.H. TO,
DAVID M. LONG, AND NATALIA ZAMBRANA PRADO

ABSTRACT. Coronal plumes are bright, narrow structures rooted in coronal holes that contribute to the solar wind. Their composition, particularly elemental fractionation as a function of first ionization potential (FIP), provides diagnostics of plasma properties and magnetic connectivity. Earlier plume studies of fractionation using low-FIP elements reached conflicting conclusions. Intermediate-FIP elements may provide additional diagnostic insight, since their fractionation is thought to involve processes beyond those affecting low-FIP species. We investigate sulfur (intermediate-FIP element) in plumes to assess the presence of fractionation, its evolution, and its relation to wave activity. We analyzed Solar Orbiter observations of two plumes in an equatorial coronal hole during March–April 2024, using Spectral Imaging of the Coronal Environment (SPICE) to derive the sulfur-to-nitrogen ratio. EUV imaging and magnetograms provided additional context. Data were processed with the open-source Python tool Spectral Analysis Fitting Framework and Reduction of Noise (SAFFRON). Both plumes showed sulfur fractionation that remained constant within uncertainties. The fractionated plasma was co-located with strong magnetic footpoints, in contrast with the surrounding interplume plasma. These results provide the evidence for sulfur fractionation in plumes and suggest, consistent with the ponderomotive force model, wave dynamics in the chromosphere as a driver.

1. Introduction

Coronal plumes are elongated, bright, and relatively narrow structures that extend from the solar surface outward through coronal holes (CHs), either polar or equatorial. They are observed in visible, extreme ultraviolet (EUV), and soft X-ray wavelengths (van de Hulst, 1950; Saito, 1965), and their structural coherence can persist up to $30 R_{\odot}$ (DeForest et al., 2001). These features are embedded in regions of open magnetic field and are hypothesized to play a role in shaping the solar corona and contributing to the solar wind, especially its fast component. Understanding their thermodynamics, dynamics, and formation mechanisms is crucial for modeling the mass and energy transport in the outer solar atmosphere.

Coronal plumes are known to be denser and cooler than the interplume region in the surrounding coronal holes (Del Zanna et al., 2008; Wilhelm et al., 2011). They also have a relatively narrow differential emission measure (DEM) profile in the corona, with emission predominantly in the range of 0.6–1.5 MK (Del Zanna et al., 2003), typically peaking near 0.8 MK, slightly cooler than the ambient coronal hole plasma at the same height (Poletto, 2015).

In addition to their thermal properties, coronal plumes have been the subject of interest in composition diagnostics. Comparing their elemental composition to in-situ solar wind measurements allows us to investigate the connectivity and mass origin of the heliospheric plasma. EUV spectroscopy enables abundance diagnostics, which in many coronal structures reveal a so-called first ionization potential (FIP) effect: an enhancement (or fractionation) of low-FIP

Date: February 27, 2026.

elements (FIP < 10 eV; e.g., K, Ca, Fe, Si) in the corona relative to the photosphere (Potasch, 1963; Meyer, 1985). In contrast, high-FIP elements (e.g., O, Ne, Ar) remain largely unfractionated.

The FIP bias is quantified as:

$$(1) \quad \mathfrak{R}_X = \frac{Ab_X^C}{Ab_X^{Ph}},$$

where Ab_X^j is the abundance of element X in the corona (C) or photosphere (Ph). With EUV observations, only relative abundance ratios between different elements X and Y are measurable:

$$(2) \quad \mathfrak{R}_{X/Y} = \frac{(Ab_X^C/Ab_Y^C)}{(Ab_X^{Ph}/Ab_Y^{Ph})}.$$

Assuming Y is a high-FIP element which has photospheric abundance ($\mathfrak{R}_Y = 1$), the fractionation ratio between X and Y is directly the FIP bias of X ($\mathfrak{R}_X = \mathfrak{R}_{X/Y}$).

Within CHs, the plasma composition is generally photospheric (Brooks & Warren, 2011; Feldman et al., 1998), consistent with measurements in the fast solar wind (Geiss et al., 1995; Mason & Bochsler, 1999; Fu et al., 2017), which originates from these regions. In contrast, enhanced FIP bias has been measured at CH boundaries (Koukras et al., 2023). These locations are believed to contribute to the slow solar wind through interchange reconnection, where closed loops outside the CHs containing fractionated plasma reconnect with open field lines, releasing the plasma into the heliosphere. While the slow solar wind is also fractionated, its composition is more variable, likely reflecting contributions from additional sources such as quiet Sun (QS) regions (Young, 2018), streamer belts (Sheeley et al., 1997), or pseudostreamers (Wang et al., 2012).

Although the overall composition within CHs is photospheric, small-scale structures embedded within them can display variable FIP bias, and plumes are a prime example. The literature on plume composition remains scarce, and the few existing studies report some contrasting results. Wilhelm & Bodmer (1998) used spectral data from the Solar Ultraviolet Measurements of Emitted Radiation (SUMER; Wilhelm et al., 1995) spectrometer onboard the Solar and Heliospheric Observatory (SoHO; Domingo et al., 1995) and reported an enhanced FIP bias in plumes based on Mg/Ne diagnostics. Using Coronal Diagnostic Spectrometer (CDS; Harrison et al., 1995) on SoHO, Young et al. (1999) measured the Mg/Ne ratio and reported an overabundance of about 1.5. However, a later study that incorporated a more accurate DEM profile for plumes questioned this interpretation (Del Zanna et al., 2003), since the characteristic narrow DEM profile of plumes can render Mg/Ne FIP bias diagnostics temperature sensitive due to the limitations of the 2-line ratio method for FIP diagnostics. More recently, Guennou et al. (2015) used the Extreme-Ultraviolet Imaging Spectrometer (EIS; Culhane et al., 2007) onboard Hinode (Kosugi et al., 2007) to analyze the Si/S abundance ratio using the DEM inversion method and found evidence that silicon is fractionated in plumes. They proposed that the FIP bias might evolve over a plume's lifetime, potentially explaining the differences between their results and those of Del Zanna et al. (2003).

The composition variability across the solar surface is a potential valuable diagnostics for assessing solar wind connectivity. By comparing in-situ composition measurements with those obtained in the source regions, it is possible to constrain the origin of solar wind streams more precisely (Brooks, 2015; Stansby et al., 2020; Yardley et al., 2023, 2024). However, the effectiveness of composition diagnostics for connectivity depends on three factors: a solid

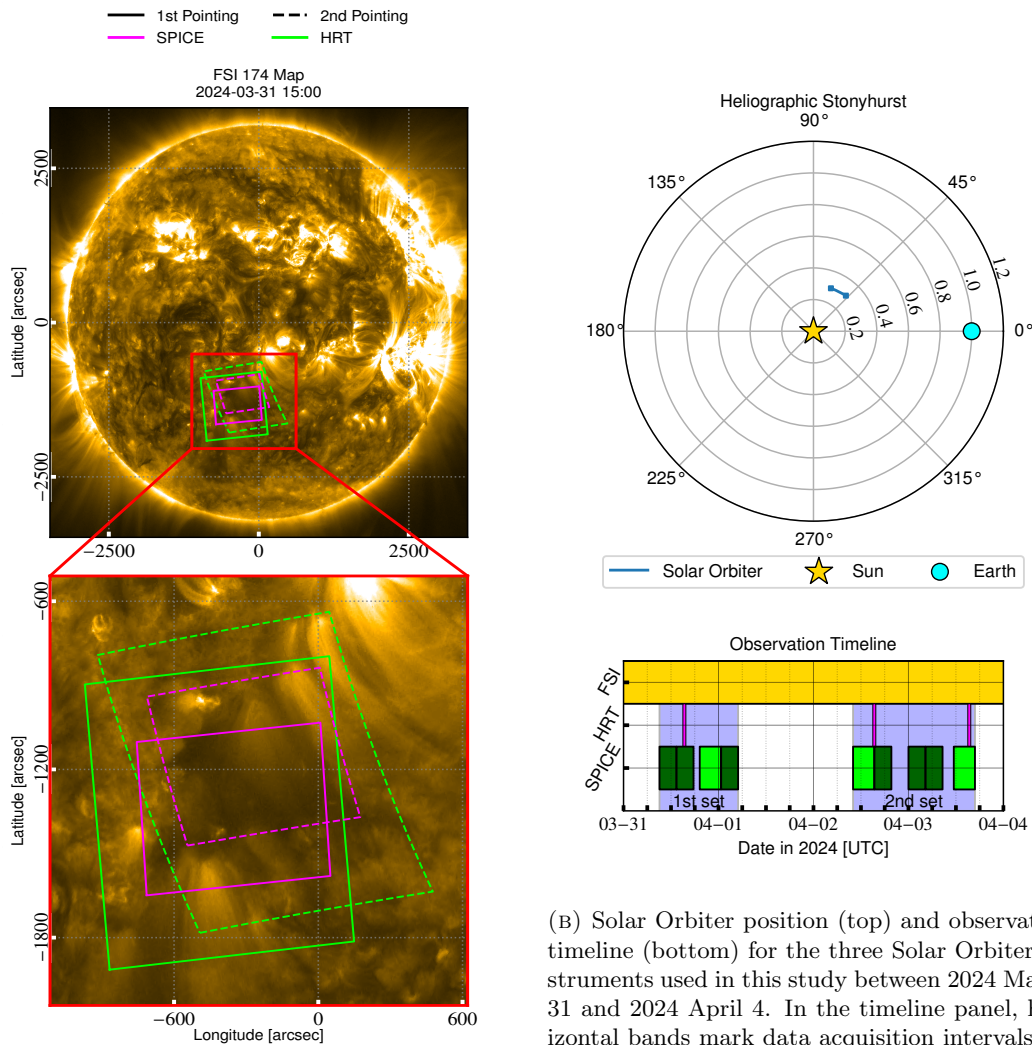
understanding of the underlying fractionation physics, the quality of both in-situ and remote-sensing data, and improved solar wind modeling. Progress in all of these areas continues to benefit from ongoing advancements.

On the theoretical side, the ponderomotive force model (Laming, 2009, 2015; Laming et al., 2019) is among the most successful frameworks for explaining FIP bias. In this model, Alfvén waves refract in the chromospheric density gradient, exerting a force preferentially on ions (mostly low-FIP elements), pushing them upward into the corona. The intermediate-FIP (mid-FIP) elements, such as sulfur, display more complex behavior, behaving sometimes as high-FIP or low-FIP elements depending on where the fractionation occurs.

Laming et al. (2019) showed theoretically that sulfur is more strongly fractionated when the ponderomotive force acts in the mid-chromosphere, a condition favored by leaking Alfvén waves from the corona, chromospheric reconnection, or wave conversion from the photosphere. Observationally, Reames (2018) reported that sulfur, along with other mid-FIP elements such as phosphorus and carbon, exhibits variable fractionation. In the fast solar wind, sulfur is generally close to photospheric values, with possible mild enhancements of order 1.1–1.3 (Laming et al., 2019). Larger values, up to ~ 2 , occur mainly in the slow solar wind and in energetic particle populations, but even in those cases sulfur remains less enriched than low-FIP species such as Fe or Si. The long-term analysis of Alterman et al. (2025) further shows that sulfur in the slow solar wind varies on solar-cycle timescales, reaching higher values during periods of increased activity. In particular, sulfur is more strongly enhanced in energetic particles from co-rotating interaction regions, whose sources are associated with slow solar wind streams, compared to gradual solar energetic particle (SEP) events thought to originate in closed coronal loops. This behaviour indicates that sulfur fractionation is sensitive to both the magnetic configuration and the wave environment of its source regions, making plume footpoints—where mixed-polarity fields and frequent reconnection events are observed (Kumar et al., 2022; Cho et al., 2023)—likely sites for sulfur enhancement.

In this study, we are interested in the behavior of sulfur (mid-FIP element, 10.36 eV) inside coronal plumes, with a particular focus on the time evolution of the FIP bias during plume development and decay. To that end, we analyze the Spectral Imaging of the Coronal Environment (SPICE; SPICE Consortium et al., 2020) data on board Solar Orbiter (Müller et al., 2020), complemented by the Solar Orbiter/Extreme-Ultraviolet Imager (EUI; Rochus et al., 2020)/Full-Sun Imager (FSI; Rochus et al., 2020) imaging and the Solar Orbiter/Polarimetric and Helioseismic Imager (PHI; Solanki et al., 2020)/High-Resolution Telescope (HRT) magnetograms. In Sec. 2, we present an overview of the observed region and introduce the instruments used in this study. We then outline the methodology used to process the spectral imaging data, with a focus on the techniques applied to the SPICE instrument (Sec. 3). Here, we also introduce our open-source data processing tool (SAFFRON¹), developed to clean and fit SPICE data for radiance and abundance map generation. The results, including the temporal and spatial evolution of the plasma composition and related observables, are presented in Sec. 4. A detailed discussion of the implications and interpretations as well as conclusions of this study are provided in Sec. 5.

¹Spectral Analysis, Fitting Framework, Reduction Of Noise Python module, <https://github.com/slimguat/saffron-spice>



(A) Context of the observations used in this study, showing the pointing coverage of SPICE (magenta) and PHI/HRT (lime) during the two observation intervals: 2024 March 31 to April 01 for the first pointing (solid), and 2024 April 2–3 for the second pointing (dashed), overlaid on the EUV/FSI₁₇₄ map from 2024 March 31 at 15:00 UT. **Top:** Full-disk EUV/FSI₁₇₄ image with overlaid pointing contours. The red box indicates the zoomed-in region shown below. **Bottom:** Zoomed view of the target CH.

(B) Solar Orbiter position (top) and observation timeline (bottom) for the three Solar Orbiter instruments used in this study between 2024 March 31 and 2024 April 4. In the timeline panel, horizontal bands mark data acquisition intervals for FSI (yellow), HRT (magenta), and each SPICE raster scan (dark green: 6'' slit; lime: 4'' slit). Shaded blue areas indicate the two main sets of CH observations. In the top panel, the Sun is at the center (yellow star), the Earth's position is at 1 AU, 0° (light blue circle), and the Solar Orbiter trajectory is shown in blue, with square markers denoting the first and last rasters (from 0.30 AU to 0.29 AU).

FIGURE 1. Observation context and timeline. (a) Context images and pointing. (b) Solar Orbiter's relative locations and instrument timeline.

2. Observational Context

2.1. Target Description The observations analyzed in this study were conducted during the Solar Orbiter Remote-Sensing Window (RSW) 14 as part of the Fast Wind Solar Orbiter Observing Plan (SOOP)², which ran from 2024 March 31 at 09:00 UT to 2024 April 3 at 21:00 UT. This SOOP also included a second observing window during RSW 15, from 2024 April 12 at 01:00 to April 16 at 06:23 UT.

The main objective of the Fast Wind SOOP is to investigate the origins of the fast solar wind, primarily associated with open-field regions such as CHs, and to connect remote-sensing observations of these sources to in-situ plasma and magnetic field measurements from Solar Orbiter or other spacecraft.

Although four distinct targets were observed during the two RSWs of the 2024 March/April Fast Wind SOOP campaign, this study focuses exclusively on the first target: a well-defined equatorial CH, observed in two intervals—from 2024 March 31 at 09:05:32 to 2024 April 1 at 04:57:10, and from 2024 April 2 at 10:00:32 to 2024 April 3 at 16:48:19. We refer to these periods as the “first” and “second” sets of observations, respectively. Figure 1a displays an EUV/FSI₁₇₄ context image from March 31 at 15:00 UT, with a zoomed view of the targeted CH shown in the bottom panel. During the observations of the target CH, Solar Orbiter was located at a distance of ~ 0.30 AU from the Sun, with a heliographic longitude between 47° and 67° relative to Earth (see Fig. 1b-top). Coordinated observations were conducted with several instruments onboard Solar Orbiter, all targeting the same CH during overlapping intervals.

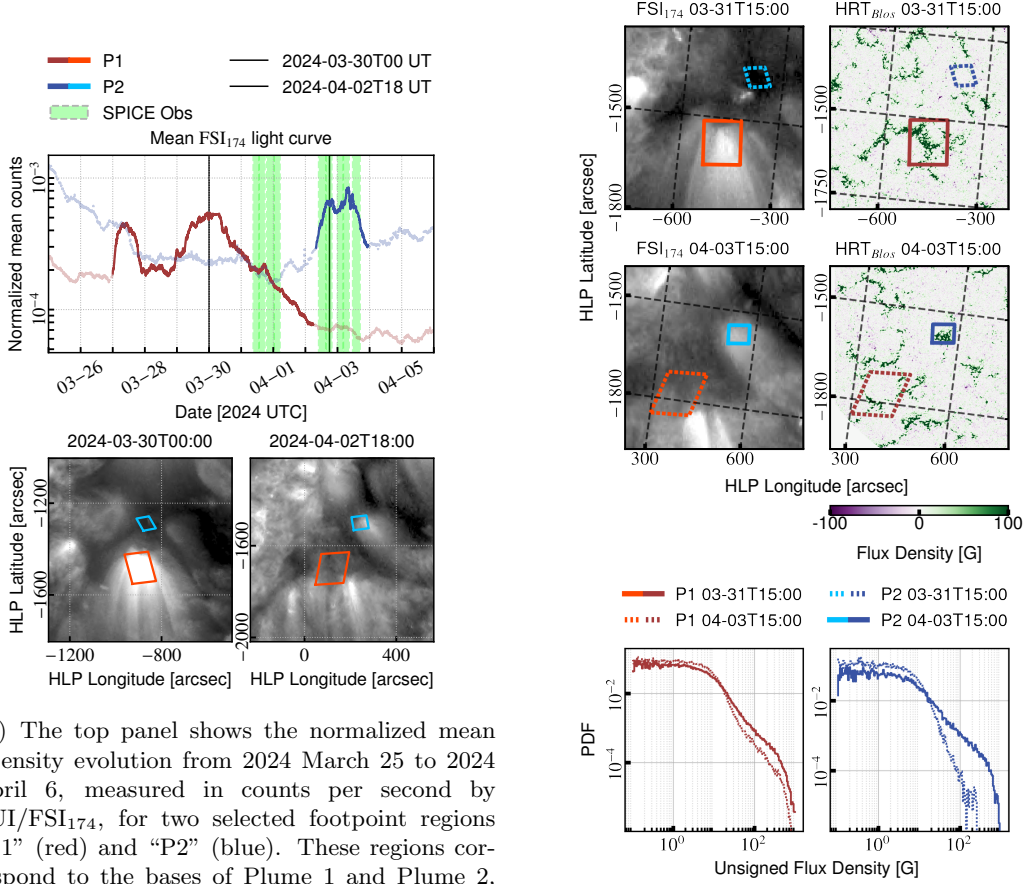
2.2. Instrumentation and Data Products This study uses the coordinated Solar Orbiter observations combining EUV imaging, spectrophotometry, and EUV spectroscopy. The EUV/FSI 174 Å channel provides full-disk images dominated by Fe IX–Fe X emission near 1 MK with a 10 min cadence, used to follow the evolution of the targeted regions. Daily PHI/HRT line-of-sight (LOS) magnetograms (15:00 UT; see bottom panel of Fig. 1b) supply the photospheric flux information and are co-aligned with EUV/FSI₁₇₄ for contextual analysis. Composition rasters from SPICE were acquired with the 4'' and 6'' slits (120 s exposures, dense rasters), producing 4–5 h scans. The two Solar Orbiter pointings were slightly offset, producing partial overlap in the narrow-field of view (FOV) instruments (Fig. 1a); HRT covered the full target CH in both cases, while SPICE sampled only part of the region, with an overlap of 56–59% between the two rasters.

The bottom panel of Fig. 1b shows the SPICE observation timeline. Dark green bars indicate raster scans with the 6'' slit and lime bars indicate scans with the 4'' slit. The number of scan steps was adjusted to keep approximately the same FOV in both cases. Four rasters were obtained during the first observation set and five during the second. The SPICE “composition” rasters include key emission lines from the transition region and low corona, used to infer elemental abundances. Details of the line selection and analysis are given in Sec. 3. In this study we exploit the L2 data from the official SPICE data release 5.0³ (SPICE Consortium et al., 2024).

2.3. Plume Identification and Evolution During the observations, we identified two plumes within the target CH (see Fig. 2a). These structures were tracked using normalized EUV/FSI₁₇₄ light curves, obtained following the processing steps described in App. D. Two fixed regions were selected in the Carrington frame and are used consistently throughout this study; we refer

²<https://www.cosmos.esa.int/web/solar-orbiter/soops-summary>

³<https://spice.osups.universite-paris-saclay.fr/spice-data/release-5.0/release-notes.html>



(A) The top panel shows the normalized mean intensity evolution from 2024 March 25 to 2024 April 6, measured in counts per second by EUI/FSI₁₇₄, for two selected footprint regions “P1” (red) and “P2” (blue). These regions correspond to the bases of Plume 1 and Plume 2, respectively, and are used consistently throughout this study. The red and blue lines are stronger over the durations in which each plume was present. The lime-colored vertical stripes indicate the times and durations of the nine SPICE raster scans targeting the same region. The bottom panels show EUI/FSI₁₇₄ context maps, in helioprojective coordinates, during the lifetimes of each plume: the bottom-left panel corresponds to Plume 1 (March 30 at 00:00 UT), and the bottom-right to Plume 2 (April 2 at 18:00 UT), with the selected regions outlined in orange and cyan.

(B) Magnetic and intensity context for the “P1” and “P2” region selections introduced in Fig. 2a. The selections are shown on the EUI/FSI₁₇₄ intensity maps (left panels) and the PHI/HRT_{BLOS} magnetograms (right panels), for both SPICE observation sets (top and bottom rows). The histogram panel shows the probability distribution function (PDF) of the unsigned magnetic flux density within the P1 (red/orange) and P2 (blue/cyan) selections, based on PHI/HRT_{BLOS} data. Solid lines indicate the time when the corresponding plume is present; dashed lines correspond to times when the plume is not present.

FIGURE 2. (a) Intensity evolution and plume context for Plume 1 and Plume 2. (b) Magnetic and intensity context of plume footprints with flux density distributions.

to them as “P1” and “P2”, the locations in which Plume 1 and Plume 2 formed. Plume 1 was

present from March 27 at 00:00 UT to April 2 at 06:00 UT, lasting about 6 days and 6 hours. Plume 2 developed later, from April 2 at 08:00 UT to April 3 at 23:00 UT, with a duration of about 1 day and 15 hours. These intervals were estimated from visual inspection of the EU1/FSI₁₇₄ images and time series, with an uncertainty of roughly 2 hours. Throughout the observing period, Plume 1 remained brighter and more extended than Plume 2. The first set of SPICE rasters, obtained on March 31 and early April 1, sampled Plume 1 during its decay. The second set, taken about one day later, covered Plume 2 shortly after its formation and throughout most of its evolution. The timing of all nine rasters is shown in Fig. 2a.

The magnetic footpoints of both regions are shown in Fig. 2b, together with the corresponding distributions of the unsigned magnetic flux density. Values below 10 G are dominated by noise (Sinjan et al. 2023 estimate a noise level of about 8.3 G under QS conditions), so only the behaviour above this threshold is meaningful. In both regions, the flux declines beyond 10 G, and during plume activity the distributions extend further toward higher field strengths, with contributions above 50 G marking the concentrated magnetic flux at the footpoints. In ‘‘P1’’, this high-field component remains visible after the decay of Plume 1, although with reduced amplitude, and its magnetic footprint is broader than that of Plume 2. When restricting the analysis to pixels above 50 G, the average unsigned magnetic flux density during plume activity is around 220 G in both regions.

3. Methods

To derive plasma parameters, we introduce the Python module Spectral Analysis, Fitting Framework, Reduction Of Noise (SAFFRON) developed for SPICE data analysis. This open-source tool encompasses multiple stages of processing, including data cleaning (e.g., despiking and cosmic ray removal, data binning), uncertainty estimation, spectral fitting, and post-processing tasks such as FIP bias diagnostics. It is designed to support both rapid inspection and in-depth analysis through in-depth fine tuning.

SPICE data preparation included cosmic ray removal using a sigma-clipping method and binning to improve the signal-to-noise ratio (SNR) (which results in $\sim 12''$ resolution in both directions). Spectral fitting was performed on both the original and binned datasets. The unbinned data retained the full spatial resolution and were used for identifying morphological structures, while the binned data provided more reliable quantitative results for composition diagnostics such as FIP bias. Example radiance maps illustrating this difference between full-resolution and binned data are shown in Fig. 7. The full description of the binning strategy, the fitting model, and the associated implementation is presented in App. A, together with the centroid constraints applied to weak or blended lines to ensure reliable fitting of the key diagnostic lines.

The full list of fitted spectral lines is given in Table 1. Also a sample of the raster windows is given in Fig. 3 where we show the wavelength-averaged image and the corresponding average spectra.

FIP bias maps were constructed using the Linear Combination Ratio method (LCR; Zambrana Prado & Buchlin, 2019), called from SAFFRON via the `fiplcr` module:

$$(3) \quad \mathfrak{R} = \frac{\sum_{i \in (\text{LF})} \alpha_i \cdot I_i / A_i^P}{\sum_{j \in (\text{HF})} \beta_j \cdot I_j / A_j^P}.$$

Line	Transition	$\log T$
Ar VIII 700.240*	$3s\ 2S_{1/2} - 3p\ 2P_{3/2}$	5.65
O III 702.337*	$2s^2 2p^2\ 3P_0 - 2s 2p^3\ 3P_1$	4.91
O III 702.838*	$2s^2 2p^2\ 3P_1 - 2s 2p^3\ 3P_0$	4.91
O III 702.896*	$2s^2 2p^2\ 3P_1 - 2s 2p^3\ 3P_1$	4.91
O III 703.855*	$2s^2 2p^2\ 3P_2 - 2s 2p^3\ 3P_2$	4.91
Mg IX 706.060	$2s^2\ 1S_0 - 2s 2p\ 3P_1$	6.00
S IV 748.393	$3s^2 3p\ 2P_{1/2} - 3s 3p^2\ 2P_{1/2}$	4.95
Mg IX 749.552*	$2s 2p\ 1P_1 - 2p^2\ 1D_2$	6.00
S IV 750.221*	$3s^2 3p\ 2P_{3/2} - 3s 3p^2\ 2P_{3/2}$	4.95
O V 760.446*	$2s 2p\ 3P_2 - 2p^2\ 3P_2$	5.32
O V 762.004*	$2s 2p\ 3P_2 - 2p^2\ 3P_1$	5.32
N IV 765.152	$2s^2\ 1S_0 - 2s 2p\ 1P_1$	5.10
Ne VIII 770.428	$1s^2 2s\ 2S_{1/2} - 1s^2 2p\ 2P_{3/2}$	5.80
Mg VIII 772.260	$2s^2 2p\ 2P_{3/2} - 2s 2p^2\ 4P_{5/2}$	5.90
S V 786.468*	$3s^2\ 1S_0 - 3s 3p\ 1P_1$	5.15
O IV 787.710*	$2s^2 2p\ 2P_{1/2} - 2s 2p^2\ 2D_{3/2}$	5.12
H I 972.537	$1s\ 2S_{1/2} - 4p\ 2P_{3/2}$	4.25
Na VI 988.709*	$2s^2 2p^2\ 3P_2 - 2s 2p^3\ 5S_2$	5.60
N III 989.799*	$2s^2 2p\ 2P_{1/2} - 2s 2p^2\ 2D_{3/2}$	4.85
N III 991.577*	$2s^2 2p\ 2P_{3/2} - 2s 2p^2\ 2D_{5/2}$	4.85
Ne VI 992.683*	$2s^2 2p\ 2P_{1/2} - 2s 2p^2\ 4P_{3/2}$	5.53

TABLE 1. Spectral lines in the SPICE composition rasters (wavelength in \AA) with their transitions and peak formation temperatures ($\log T$). Blended lines are marked with *.

Here, α_i and β_j are coefficients for low- and high-FIP lines, and A^P denotes photospheric abundances obtained by [Grevesse et al. \(2007\)](#). The atomic physics data are obtained using CHIANTI atomic database (version 11.0.2, [Dere et al., 1997](#); [Dufresne et al., 2024](#)). HF denotes the lines of the elements considered as high-FIP, while LF is for the lines of elements considered as low-FIP.

These coefficients were optimized using the CHIANTI-provided typical DEMs for active regions, coronal holes, and quiet Sun. While [Zambrana Prado & Buchlin \(2019\)](#) found that the LCR method is relatively insensitive to the DEM choice, it requires that the selected lines have sufficiently similar contribution functions to allow the cost function (Eq. 21 in [Zambrana Prado & Buchlin \(2019\)](#)) to reach a well-defined minimum.

The selected lines from a high-FIP element are N IV 765.152 \AA and N III 991.577 \AA , and the lines from a lower-FIP element are S IV 750.221 \AA and S V 786.468 \AA . Their contribution functions peak around 0.08–0.15 MK, as shown in Fig. 4, corresponding to transition region temperatures. All of the selected spectral lines are considered optically thin including N III 991.577 \AA . Previous studies have shown that this line with a low formation temperature remains optically thin in coronal holes including plume footpoints ([Jordan et al., 2001](#); [Varesano et al., 2024](#)). A dedicated analysis of the S/N composition diagnostics with SPICE, also part of this special issue ([Zambrana Prado et al., 2025](#)), further assesses the performance of the LCR method for these line ratios.

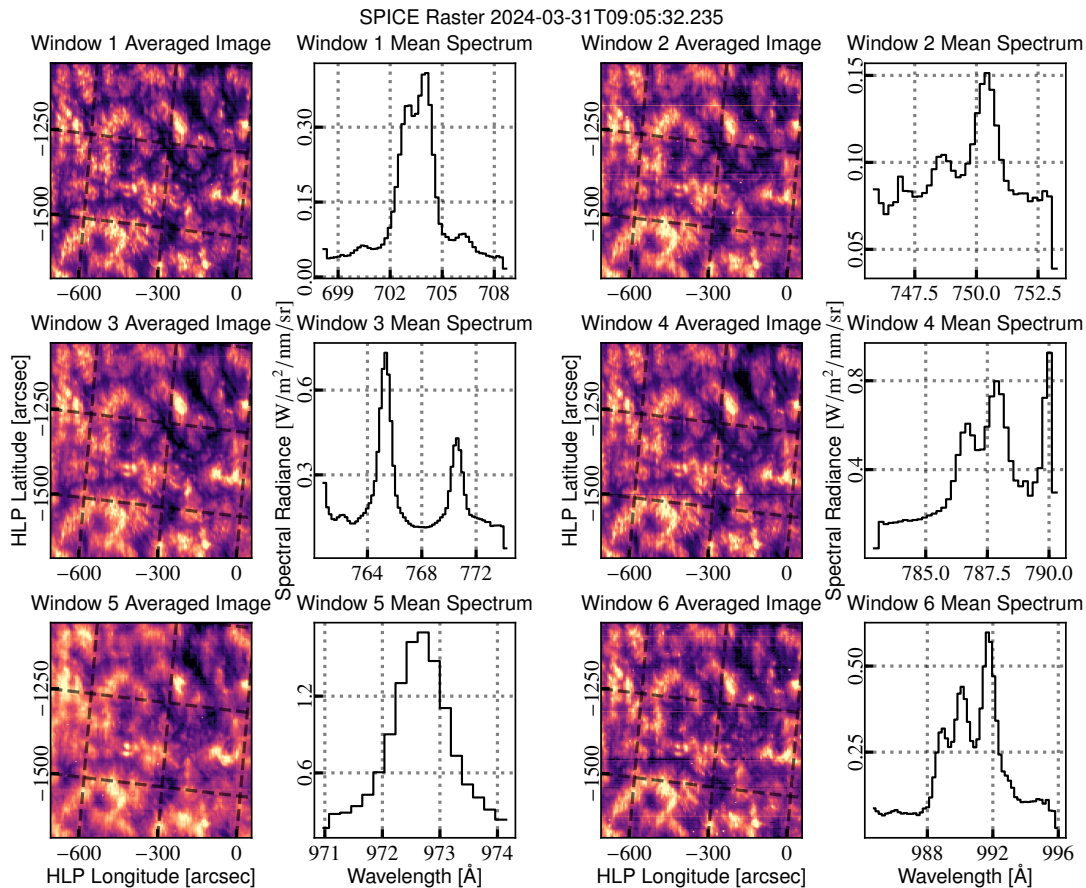


FIGURE 3. Sample SPICE composition raster from 2024 March 31 at 09:05:32 UT. First and third columns show mean images for each of the six spectral windows (window 1 to window 6), averaged along wavelength dimension. Right to each image panel we show the corresponding average spectra per window across the spatial axis.

To apply the LCR method to the SPICE data, we adopted a fixed electron density of 10^{10} cm^{-3} . In principle, density diagnostics are available in the SPICE range through the O V 761.128 \AA /760.446 \AA ratio. However, this interval also contains three nearby O V lines that form a blended group, and in our dataset this part of the spectrum falls at the edge of the spectral window (see Fig. 3, Window 3 mean spectrum). The full set of lines is therefore not captured, making the O V ratio unreliable for density estimation.

A value of 10^{10} cm^{-3} is an upper bound for typical transition-region conditions in CHs (Doschek et al., 1997). Since higher assumed densities reduce the inferred FIP bias, this choice results in a conservative estimate; any measured enhancement above the uncertainties can be regarded as real and possibly stronger than reported. Density-related considerations are discussed further in App. B.

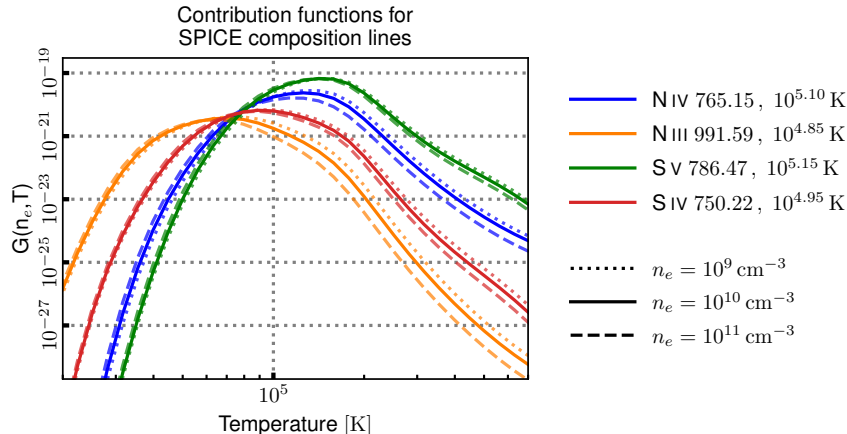


FIGURE 4. Contribution functions (in $\text{erg cm}^3 \text{s}^{-1} \text{sr}^{-1}$) for the SPICE composition lines used in this study, computed with CHIANTI v.11 (using the IDL package of CHIANTI) for three constant electron densities of 10^9 , 10^{10} , and 10^{11} cm^{-3} . Each curve is labeled with the ion, wavelength (in \AA), and T_{max} , the peak formation temperature, in K.

To improve the SNR, composition maps were generated from binned data, and pixels with relative uncertainties exceeding 50% were excluded from the FIP bias analysis. Here, the relative uncertainty refers to the ratio of the propagated intensity error to the fitted line intensity, where the intensity errors are obtained by propagating uncertainties arising from photon statistics and from the instrument’s broad point spread function (PSF), which also deviates slightly from a Gaussian profile. These effects dominate over other sources of error, such as uncertainties in atomic data (from CHIANTI v.11, [Dufresne et al., 2024](#)) or radiometric calibration ([SPICE Consortium et al., 2024](#)). The resulting relative uncertainties on the fitted line intensities directly provide the error estimates on the derived FIP bias values. The full uncertainty calculation and propagation procedure is described in App. C.

4. Results

4.1. FIP bias within plumes Figure 5 shows the resulting FIP bias maps (first row) and selected SPICE radiance maps (subsequent rows) for four selected raster scans, one per column. The first two scans were acquired during the March 31 pointing, and the last two during the April 2–3 pointing. The radiance maps are ordered by peak emission temperature: N III 765.152 \AA (0.15 MK), Ne VIII 770.428 \AA (0.63 MK), and Mg IX 706 \AA (1.00 MK). The FIP bias maps trace the plasma composition between 0.1 MK and 0.15 MK.

The FIP bias across the full SPICE FOV ranges between 0.8 and 1.0, indicating that sulfur remains close to its photospheric abundance. However, the “P1” region in Fig. 5, corresponding to the location of Plume 1 footpoint, shows consistent fractionation during the first observation set (first and second columns), with FIP bias values between 1.1 and 1.5. During these observations, Plume 1 is clearly visible in the Mg IX maps. In the second observation set (third and fourth columns), “P1” lies mostly outside the SPICE FOV, and is therefore excluded from further analysis.

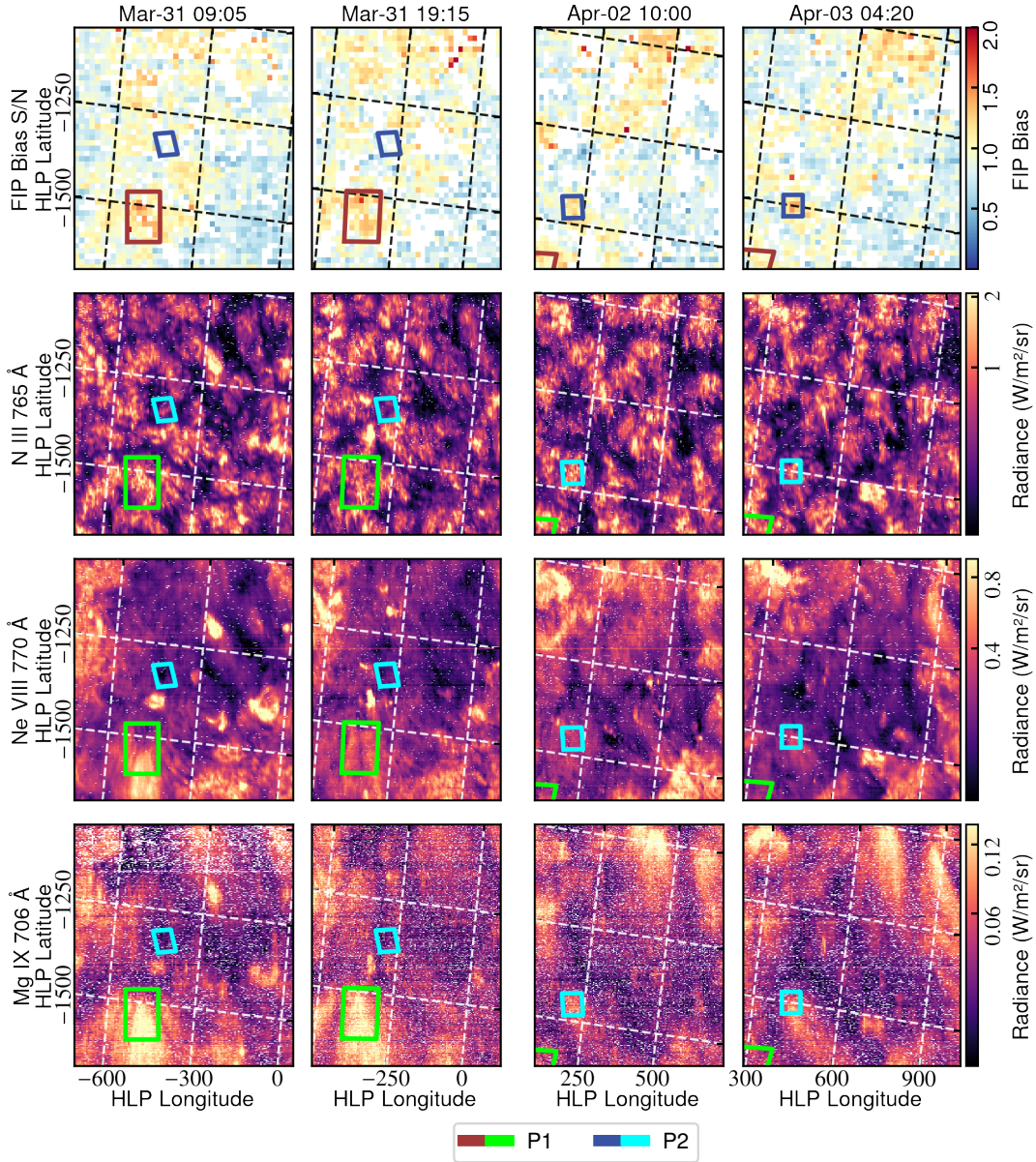


FIGURE 5. Sample of SPICE observations from each observation set: the first set is shown in the first two columns, and the second set in the last two columns. Each column displays, from top to bottom, the S/N FIP bias maps and radiance maps for SPICE N III (used in the FIP bias calculation; low-TR), Ne VIII (top-TR), and Mg IX (corona). The regions labeled “P1” (red in the FIP bias maps and green in the radiance maps) and “P2” (blue in the FIP bias maps and light blue in the radiance maps) indicate the locations of Plume 1 and Plume 2, respectively. These regions were selected based on visual identification of the plume footpoints in one map and propagated to the others by fixing the Carrington coordinates of the region vertices.

The “P2” region shows fractionation only during the second observation set (starting from April 2), corresponding to the presence of Plume 2. The plume is then visible in Mg IX maps. In contrast, during the first set—prior to the appearance of Plume 2—the FIP bias in this region is approximately 1.0, consistent with photospheric sulfur abundance. In both plumes, the fractionated areas align with enhanced N III emission in the plume footpoints.

Although Plume 1 was observed (during the first set of observations) in its decay phase, its structure remains clearly detectable in Mg IX, as shown in the fourth row of Fig. 5. The Ne VIII maps, however, reveal temporal variations in the emission from Plume 1 (first and second column of Fig. 5), with the weakest signal recorded on March 31 at 19:15. This suggests thermal evolution of the plume structure at transition region temperatures. Plume 2 was observed throughout its lifetime but appears smaller and systematically fainter in Ne VIII. A lower emission measure at this temperature may arise from a cooler thermal distribution and/or a reduced plasma density; both interpretations are consistent with Plume 2 being intrinsically weaker than Plume 1.

4.2. In-depth Plume FIP bias analysis and error analysis The FIP bias enhancements observed in the “P1” and “P2” regions originate from the footpoints of Plume 1 and Plume 2. However, we focus solely on assessing the presence of sulfur fractionation rather than deriving precise FIP bias values, due to the lack of precise electron density diagnostics as detailed in Sec. 3. Because of the assumed density, the reported FIP bias values should be regarded as conservative lower limits. Thus, whenever the measured FIP bias exceeds unity by more than its associated uncertainty, this indicates genuine sulfur enrichment. Consequently, values near or below unity are interpreted as photospheric. In particular, we emphasize that the values below one are not indicative of an inverse FIP (IFIP) effect, as they could be the outcome of the density assumption.

Figure 6a illustrates the FIP bias measurements and associated uncertainties across the selected areas “P1” and “P2” during two sets of SPICE observations. These distributions allow us to assess the spread in composition values and the reliability of the inferred FIP bias in each plume over time. To distinguish reliably fractionated pixels from those consistent with photospheric composition, we applied the criterion $\mathfrak{R} - \Delta\mathfrak{R}/2 > 1$, where \mathfrak{R} is the measured FIP bias and $\Delta\mathfrak{R}$ its uncertainty. Pixels satisfying this condition are represented in the green-shaded domain of the scatter plots and are considered confidently fractionated. The fraction of such pixels can be visually tracked across scans and directly compared between Plume 1 and Plume 2.

In the first observation set, the “P1” histograms show a clear population of fractionated pixels, with values typically around 1.2 and reaching up to 2.0. Conversely, the “P2” region displays a clear FIP bias enhancement during the second observation set when Plume 2 is present, with values reaching up to 1.5. No such signature is present in the first set, prior to the appearance of Plume 2.

These findings indicate that sulfur becomes fractionated in the presence of plumes, while it remains photospheric prior to the Plume 2 formation.

4.3. FIP bias evolution over time After confirming that the targeted plumes exhibit sulfur fractionation, we quantify the FIP bias evolution over time for both regions “P1” and “P2”. To achieve this, we compute the weighted mean FIP bias within each region using the following

expression:

$$(4) \quad \bar{\mathfrak{R}} = \frac{\sum_i^N \mathfrak{R}_i \cdot \frac{1}{\Delta \mathfrak{R}_i^2}}{\sum_i^N \frac{1}{\Delta \mathfrak{R}_i^2}},$$

where \mathfrak{R}_i and $\Delta \mathfrak{R}_i$ denote the FIP bias and its estimated uncertainty for pixel i .

Figure 6b presents the results. The top row shows the time evolution of the weighted mean FIP bias, while the bottom panels reproduce the normalized light curves from Fig. 2a, now zoomed into the SPICE observation windows.

We find that the mean FIP bias during the lifetime of both plumes is around 1.2, occasionally reaching up to 1.3. Both regions show comparable fractionation behavior. Notably, the FIP bias in ‘‘P2’’ remains photospheric prior to the appearance of Plume 2 and six hours after its appearance, the average FIP bias indicates clear enrichment, and continues to increase further in the following observation, which occurs 10 hours after the plume’s appearance. The FIP bias then stabilizes until the final observation, which took place seven hours before the complete decay of the plume.

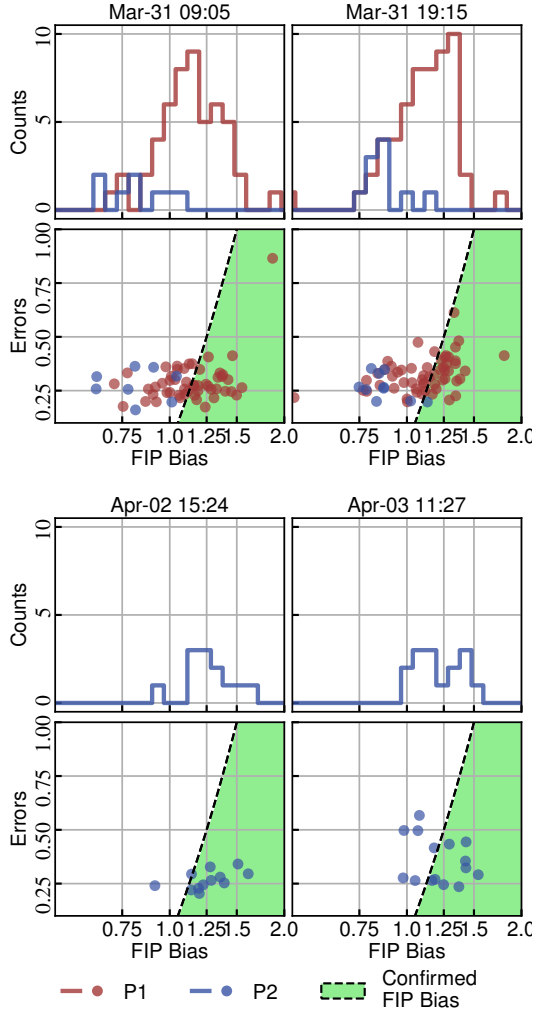
As previously mentioned, the assumed electron density of 10^{10} cm^{-3} provides a conservative lower limit of the FIP bias. If we consider a broader range down to the lower CH density of 10^9 cm^{-3} , the actual FIP bias could be $\sim 20\%$ higher, bringing peak values close to 1.4 or more.

5. Discussions and Conclusion

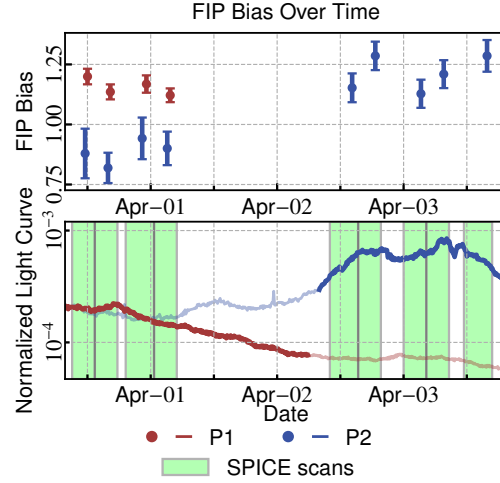
Our results clearly indicate that sulfur undergoes fractionation inside the observed plumes. Both plumes show comparable overall FIP bias levels; however, the fractionated area is larger in Plume 1. This correlates with Plume 1 being more intense (Fig. 2a) and having a larger and stronger magnetic flux concentration (exceeding 100 G; Fig. 2b).

Throughout the lifetime of each plume, no time-dependent variation of the FIP bias was detected — at least not within the measurement uncertainties. However, a distinct increase in FIP bias is observed at the location of Plume 2 between its pre-formation phase and active phase. Between March 31–April 1 and April 2–3, the FIP bias increased from approximately 0.9 to 1.2, indicating that sulfur became fractionated within the six hours leading up to the first SPICE observations of the plume. Because we assume a relatively high electron density for a coronal hole environment in our analysis, the derived FIP bias values represent conservative lower limits. Accounting for this, the actual FIP bias in the plumes could be 10–20% higher. A slight variation is observed in Plume 2 during its activity, but it remains almost within the uncertainties of the measurements.

This sulfur fractionation behavior can be interpreted with the ponderomotive force model (Laming, 2009, 2015), in which the FIP bias is produced by the ponderomotive acceleration. This acceleration scales with the gradient of the transverse wave electric energy, $\partial \delta E_{\perp}^2 / \partial z$, and is directed upward, from the chromosphere towards the corona. Under such conditions, the ponderomotive force peaks near the top of the chromosphere. Laming et al. (2019) also demonstrated that mid-FIP fractionation, including sulfur, is possible if Alfvén waves penetrate into the mid-chromosphere. In their model, one source of these waves is coronal Alfvén waves that partially transmit through the density barrier of the TR, reaching the upper chromosphere where the ponderomotive force is generated. Moreover, torsional Alfvénic waves can propagate deeper into the mid-chromosphere, thereby enabling mid-FIP fractionation. Alfvén waves may also be generated directly within the chromosphere, since reconnection can take place at multiple atmospheric heights (Raouafi et al., 2023), or they may arise from upward-propagating



(A) FIP bias distribution and uncertainty analysis for pixels in the plume footpoint regions “P1” (red) and “P2” (blue). Each vertical pair of histogram and scatter plot corresponds to a raster scan selected as in Fig. 5. The top two pairs represent the first SPICE observation set (March 31), and the bottom four pairs represent the second set (April 2–3). In each pair: **Top panel** shows the FIP bias histogram; **Bottom panel** shows the scatter plot of FIP bias versus uncertainty. The dashed black line marks the threshold $\mathfrak{R} - \Delta\mathfrak{R}/2 = 1$; pixels in the green-shaded region are considered reliably fractionated.



(B) Temporal evolution of the FIP bias in regions “P1” (red) and “P2” (blue), corresponding to the footprints of Plume 1 and Plume 2. **Top panel:** Weighted mean FIP bias in each region, derived from the maps in Fig. 5 and the distributions in Fig. 6a, using Eq. 4. Each point is associated with the average scan time of the relevant sub-region. **Bottom panel:** Normalized mean intensity evolution from EU1/FSI₁₇₄ during the SPICE observation period. Lime bars indicate the time windows of the SPICE rasters, as in Fig. 2a.

FIGURE 6. (a) FIP bias distributions and uncertainty analysis for plume footpoint regions P1 and P2. (b) Temporal evolution of the weighted mean FIP bias and corresponding intensity variations in the same regions.

waves originating in the photosphere through slow-to-Alfvén (Khomenko & Cally, 2012) or fast-to-Alfvén (Jess et al., 2012; Chae et al., 2021) mode conversion. Although Alfvén waves converted from p modes leaking into plume regions have been reported as quasi-periodic 3–5 minute activity in the corona (Kumar et al., 2022), Chae & Lee (2023) showed that in quiescent conditions (non-flaring Sun), upward waves alone do not generate a significant ponderomotive force.

It is therefore reasonable, based on the predictions of the ponderomotive-force model, to expect plume plasma to undergo fractionation. Plumes are not single monolithic structures, but rather the collective outcome of numerous small-scale events, often referred to as plumelets (Uritsky et al., 2021; Kumar et al., 2022). Each plumelet forms through the reconnection of background open-field lines with small closed loops rooted in mixed-polarity magnetic patches, where the main dominant polarity interacts with parasitic inverse polarities, as found by Cho et al. (2023) using high-resolution observations from BBSO/NIRIS. These reconnection events generate small-scale plasma jets, or jetlets (Raouafi & Stenborg, 2014; Panesar et al., 2018), which collectively sustain the large-scale plume structure (Raouafi et al., 2023). The reconnection dynamics naturally excite Alfvénic perturbations. In this framework, the observed plume fractionation can be understood as a consequence of the ponderomotive force acting on plasma in the upper and mid-chromosphere. The same dynamics that sustain plume activity also supply the necessary Alfvénic amplitudes. These are absent in inter-plume regions, which explains why the CH plasma generally lacks fractionation signatures (Feldman et al., 1998). A fraction of these perturbations are torsional Alfvén waves, which can penetrate deeper into the chromosphere and provide a natural explanation for the sulfur enhancement that we observe.

In this study, we do not have direct access to wave diagnostics in the chromosphere, which prevents us from directly constraining the role of chromospheric wave activity in the observed fractionation. Specifically, we cannot quantify the wave energy, determine its latitudinal gradients, or assess its polarization. Nor can we confirm which processes act as the dominant sources of the waves. These limitations highlight the need for future observations with high spatial and temporal resolution, both in the chromosphere and the lower corona, to firmly establish the connection between chromospheric wave properties and fractionation signatures.

Guennou et al. (2015) analyzed Si/S fractionation using Hinode/EIS data and found silicon enhanced over sulfur by a factor of 1.1 to 1.3. However, because our results suggest sulfur itself is fractionated in plumes, their silicon enrichment might be underestimated. If sulfur is enhanced to the degree we observed, the true ratio of silicon to a typical low-FIP element (e.g., O, Ne, Ar) would be higher (up to 1.7). It is also possible that plume cases where the Si/S ratio is close to unity do not reflect an absence of silicon fractionation, but rather comparable fractionation of both silicon and sulfur.

That study also investigated temporal variability and found that the FIP bias remained constant over time for three out of four plumes, while one displayed a clear time-dependent evolution. Furthermore, plumes that decayed were found to revert to interplume (i.e., photospheric) composition — a similar trend we observe in the FIP bias of region “P2” before (first set) and during (second set) Plume 2 activity. Although we detect no significant temporal evolution in the FIP bias of our studied plumes, such variability may depend on plume-specific properties that modulate the wave energy content and the generation of Alfvén waves, thereby influencing the fractionation rate. A larger statistical sample may be required to identify consistent trends. If FIP bias is indeed modulated by the occurrence and amplitude of Alfvén waves, then plumes with more dynamic evolution or changing magnetic configurations may exhibit stronger time variability. Notably, the most pronounced changes in fractionation must

occur during the early phases of plume formation or during their decay (within a few hours at most).

Based on the sulfur fractionation observations in our results, together with the theoretical predictions of the ponderomotive-force model (Laming, 2009, 2015; Laming et al., 2019), it is possible that the combination of mid-FIP and low-FIP abundance enhancements could serve as an indirect proxy for the presence and transport of Alfvén waves in the mid-chromosphere. It might also enable direct linkage between in-plume composition and solar wind observations. However, in this study, we lack connectivity with in-situ instruments and therefore cannot establish such links (Stansby et al., 2020).

To investigate the role of small-scale structures in FIP bias formation, coordinated multi-instrument observations with both high spatial and temporal resolution are essential. On one side, high-resolution (resolving down to plumelet scale, ~ 100 km at large) EUV spectrometers capable of diagnosing transition region and coronal plasma properties — including composition — are required, such as the forthcoming Solar-C (Watanabe, 2014) mission and its spectral imager EUV Spectroscopic Telescope (EUVST; Shimizu et al., 2020). These should be complemented by high-cadence EUV imaging, for example with Solar Orbiter/EUI/High-Resolution Imager (HRI; Rochus et al., 2020), to capture the global coronal dynamics and small-scale structures. On the other side, high-resolution measurements from advanced ground-based telescopes — such as Goode Solar Telescope (GST; Cao et al., 2010) or Daniel K. Inouye Solar Telescope (DKIST; Tritschler et al., 2015) — are essential for the detection of Alfvén waves in the chromosphere as well as for resolving the fine-scale magnetic structures at plume footpoints (below 100 km) and characterizing the chromospheric environment (Jess et al., 2009; Srivastava et al., 2017; Murabito et al., 2024). This would provide constraints on the chromospheric wave energy content and polarization, allowing direct comparison with coronal FIP bias measurements and improving the current FIP bias models.

Acknowledgements

S.M. acknowledges funding from the Université Paris-Saclay EDOM doctoral scholarship. This work was supported by the Paris Region via the DIM Origines funding. S.M. and M.J. acknowledge support from the European Space Agency (ESA) Archival Research Visitor Programme. D.B. is funded under Solar Orbiter EUI Operations grant number ST/X002012/1 and Hinode Ops Continuation 2022-25 grant number ST/X002063/1. N.Z.P. is supported by STFC Consolidated Grant ST/W001004/1. A.S.H.T. is supported by the ESA Research Fellowship. Solar Orbiter is a space mission of international collaboration between ESA and NASA, operated by ESA. We are grateful to the ESA SOC and MOC teams for their support. The development of SPICE has been funded by ESA member states and ESA. It was built and is operated by a multinational consortium of research institutes supported by their respective funding agencies: IAS (Centre National d’Etudes Spatiales (CNES), operations lead), STFC RAL (the UK Space Agency (UKSA), hardware lead), GSFC (NASA), MPS (Deutsches Zentrum für Luft- und Raumfahrt (DLR)), PMOD/WRC (Swiss Space Office (SSO)), SwRI (NASA), UiO (Norwegian Space Agency). The EUI instrument was built by CSL, IAS, MPS, MSSL/UCL, PMOD/WRC, ROB, LCF/IO with funding from the Belgian Federal Science Policy Office (BELSPO/PRODEX PEA 4000112292 and 4000134088), CNES, UKSA, the Bundesministerium für Wirtschaft und Energie (BMWi) through DLR; and SSO. The German contribution to SO/PHI is funded by the BMWi through DLR and by MPG central funds. The Spanish contribution is funded by AEI/MCIN/10.13039/501100011033/ and European

Union “NextGenerationEU”/PRTR” (RTI2018-096886-C5, PID2021-125325OB-C5, PCI2022-135009-2, PCI2022-135029-2) and ERDF “A way of making Europe”; “Center of Excellence Severo Ochoa” awards to IAA-CSIC (SEV-2017-0709, CEX2021-001131-S); and a Ramón y Cajal fellowship awarded to DOS. The French contribution is funded by CNES. This work used data provided by the MEDOC data and operations centre (CNES / CNRS / Université-Paris-Saclay), <https://idoc.osups.universite-paris-saclay.fr/medoc/>. CHIANTI is a collaborative project involving George Mason University, the University of Michigan (USA), University of Cambridge (UK) and NASA Goddard Space Flight Center (USA). The authors would like to thank Susanna Parenti, Teodora Mihailescu and Ramada Sukarmadji for fruitful discussions and invaluable insights. We also thank Luca Franci and Clara Froment for their coordination of the SOOP observations used in this study and for their valuable input and discussions. We thank the referees for their constructive comments, which significantly improved the quality and clarity of this work prior to publication. We acknowledge the use of the following Python libraries: version 7.0 of the SunPy open source software package, Astropy, a community-developed core Python package and an ecosystem of tools and resources for astronomy, as well as the Numpy and Scipy libraries. We acknowledge the use of the following software in this work: the `fiplcr` package for FIP-bias diagnostics using the Linear Combination Ratio method (Zambrana Prado & Buchlin, 2019); EISPAC for Hinode/EIS data analysis (Weberg et al., 2023); NumPy (Harris et al., 2020); SciPy (Virtanen et al., 2020); Matplotlib (Hunter, 2007); and the `multiprocess/pathos` libraries for parallel execution (McKerns et al., 2012).

A. SPICE Binning and Spectral Fitting Procedure

Binning kernels were adjusted depending on the raster step size. For the 4''-step rasters, data were binned by 3 pixels in the raster x -direction (slit scanning direction) and 13 pixels along the y -direction. For the 6''-step rasters, only 2 pixels were binned in x -direction to get a closer resolution between the two study types. This choice maintains a comparable binned pixel size of roughly 12'' across both study types and in both spatial directions. Figure 7 shows sample SPICE radiance maps of N IV, Ne VIII, and Mg IX, obtained by fitting the original data (top) and the binned data (bottom).

Uncertainty estimates for the SPICE line intensities were computed using the `spice_error()` routine in the `sospice` Python package, following the methodology detailed in App. A of Huang et al. (2023).

Each spectral window was fitted with a multi-Gaussian function:

$$(5) \quad F(\lambda; \{I_i\}_{i=1}^N, \{\lambda_i\}_{i=1}^N, \{\sigma_i\}_{i=1}^N, B) = B + \sum_{i=1}^N I_i \cdot e^{-\frac{(\lambda-\lambda_i)^2}{2\sigma_i^2}}$$

where N is the number of emission lines per window, B is the background level, and I_i , λ_i , and σ_i represent the intensity, centroid, and width of the i -th Gaussian, respectively. Fitting was performed using SciPy’s `curve_fit`.

Blended lines crucial for further analysis were treated with constrained fitting. For example, S IV 750.221 Å is blended with Mg IX 749.552 Å. These were disentangled using fixed wavelength offsets relative to other lines of the same ionization state that are not blended, namely S IV 748.393 and Mg IX 706.060. The centroid constraints are described as such:

$$(6) \quad \lambda_{\text{S IV } 750.221} = \lambda_{\text{S IV } 748.393} + \Delta\lambda_{\text{S}}$$

$$(7) \quad \lambda_{\text{Mg IX } 749.552} = \lambda_{\text{Mg IX } 706.060} + \Delta\lambda_{\text{Mg}}$$

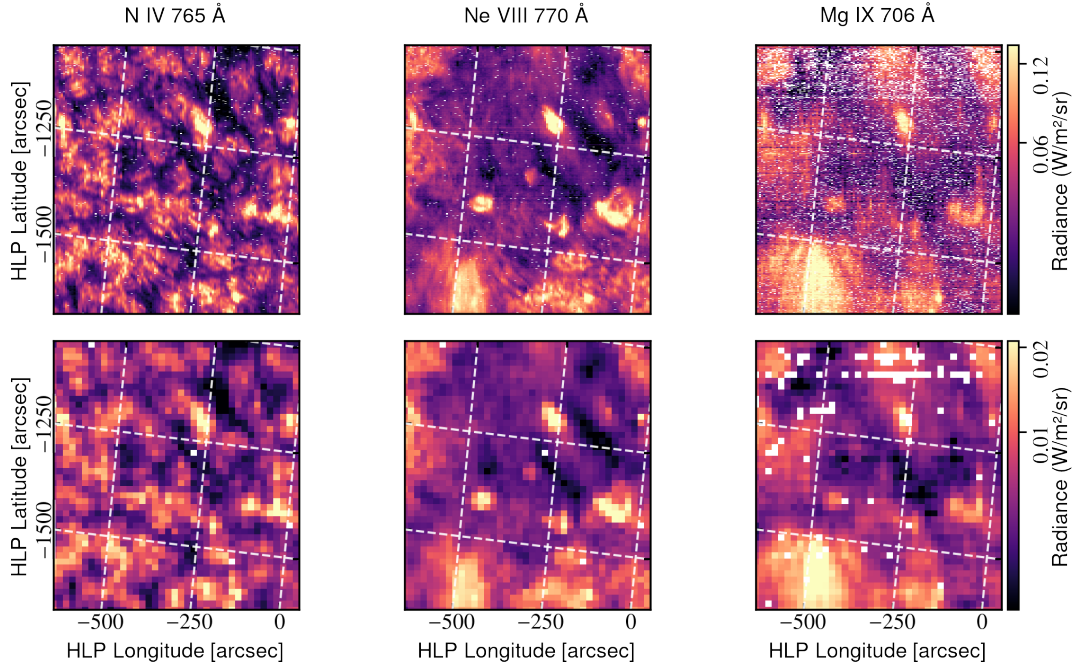


FIGURE 7. Sample SPICE radiance maps from March 31 at 09:05, shown for N IV 765.152 Å (one of the lines used for the composition diagnostics), Ne VIII 770.428 Å, and Mg IX 706.060 Å. The top row displays the full-resolution maps, and the bottom row shows the corresponding binned maps.

where $\Delta\lambda_S$ and $\Delta\lambda_{Mg}$ are theoretical separations (NIST atomic database version 5.12, [Kramida et al., 2024](#); [Martin et al., 2023](#)), between the blended and non-blended lines.

Similarly, the weak blended lines Fe III 985.852, Ne VI 992.683, and Fe III 994.258 were fitted with centroid constraints relative to N III 991.577. This approach prevents contamination of the N III line profile by nearby low-intensity lines and provides a more reliable estimate of the local background. The two Fe III lines lie at the edges of the spectral window and are therefore not always fully captured.

B. Density Effects on the FIP Bias

The FIP bias values computed in this work rely on a fixed choice of electron density. In this section, we detail the assumptions adopted, justify their use in the context of plume fractionation, and examine how varying the density affects the resulting FIP bias.

Since the SPICE dataset we used lacked the density-diagnostic lines, we adopted fixed values within the expected CH density range. To remain conservative, we selected a relatively high value of 10^{10} cm^{-3} —representative of the upper limit typically found in the transition region of CHs ([Doschek et al., 1997](#); [Del Zanna & Bromage, 1999](#)). This choice tends to minimize the estimated sulfur FIP bias, as the N IV line used in our diagnostic is density-sensitive and produces lower FIP bias values at higher densities as we are going to show.

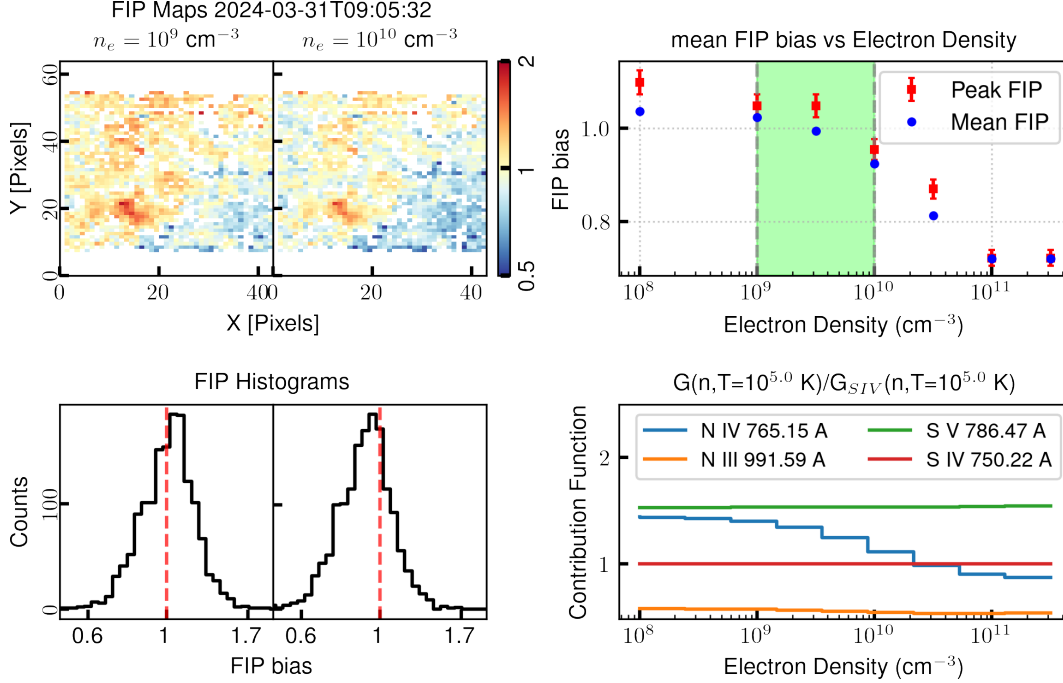


FIGURE 8. Effect of electron density on sulfur FIP bias derived from SPICE data. **Left column:** FIP bias maps (top) and corresponding histograms (bottom) for two representative electron densities: $n_e = 10^9 \text{ cm}^{-3}$ and $n_e = 10^{10} \text{ cm}^{-3}$, highlighting the impact of density assumptions on both spatial distribution and statistical spread of the FIP bias. **Top-right:** Mean (blue circles) and histogram peak (red squares) FIP bias values as a function of electron density. Error bars on the peak values denote bin widths. The shaded green area marks the coronal hole density range. **Bottom-right:** Normalized contribution functions $G(n, T = 10^{5.0} \text{ K})/G_{SIV}(n, T = 10^{5.0} \text{ K})$ of selected spectral lines.

With this conservative approach, any fractionation signal observed is a lower bound. If real electron densities are lower, the true FIP bias would be higher. Figure 8 illustrates this sensitivity. FIP bias maps are shown for the two boundaries of the expected CH density range, revealing a consistent trend: lower densities yield higher FIP bias values. This trend is also reflected in the corresponding histograms, where both the peak and mean shift toward higher values as density decreases.

The top-right panel of Fig. 8 summarizes this behavior. It shows the mean and peak FIP bias as a function of assumed electron density, across a range from 10^8 to $10^{11.5} \text{ cm}^{-3}$. Most values converge near unity within the green-shaded region, which marks the typical CH density range. This consistency further supports the plausibility of our fixed-density approach.

Among the selected spectral lines, N IV 765.152 Å is the density-sensitive line in this collection which is shown in the bottom-right panel of Fig. 8, that shows the normalized theoretical $G(n, T)$ (relative to that of S IV) at $T = 10^5 \text{ K}$. The contribution of the N IV line changes significantly

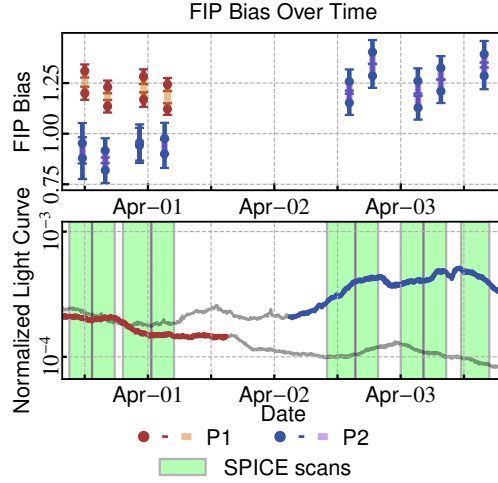


FIGURE 9. Same as Fig. 6b, but now also showing the FIP bias computed assuming an electron density of 10^9 cm^{-3} (filled markers above each original point). Additional vertical error bars (in orange for “P1” and in purple for “P2”) represent the uncertainty introduced by varying the assumed electron density between 10^9 and 10^{10} cm^{-3} , highlighting the impact of density assumptions on the FIP bias.

for $n_e > 10^{9.5} \text{ cm}^{-3}$, while the other lines remain largely unaffected by density. This confirms that the NIV line is the dominant source of density dependence in our FIP diagnostic. For the time being, this method provides the most practical way to identify sulfur fractionation signatures under the current constraints.

To assess how the density assumption affects the temporal evolution of the FIP bias, we take Fig. 6b, which displays the time series of the weighted mean FIP bias in “P1” and “P2”, and present in Fig. 9 the same quantities recalculated using both the upper and lower bounds of the CH density range (10^9 – 10^{10} cm^{-3}). Under the lower density assumption, FIP bias values in both regions increase, with some reaching above 1.4. In particular, the non-fractionated state of “P2” prior to plume appearance is then consistent with CH expectations (bias close to unity).

C. Error estimation

C.1. Error Estimation from Spectral Line Fitting Spectral line intensities are derived from Gaussian fitting performed using the `curve_fit` function from the `scipy.optimize` Python library. This routine implements the Levenberg–Marquardt algorithm (Levenberg, 1944; Marquardt, 1963) for non-linear least-squares minimization. Crucially, the fitting procedure incorporates pixel-level statistical uncertainties from the data cube during the fit.

These statistical uncertainties are computed using the `spice_error` function from the `sospice` Python module (see [Huang et al., 2023](#)). If spectral binning is applied to improve signal-to-noise, the variances are propagated as:

$$(8) \quad \Delta f_{\text{bin}} = \sqrt{\frac{1}{N^2} \sum_{i=1}^N (\Delta f_i)^2},$$

where Δf_i are the individual pixel uncertainties and N is the number of pixels combined. This ensures correct weighting during the fit.

The fitting process returns both the best-fit parameters and their 1σ uncertainties derived from the square root of the diagonal of the covariance matrix. For each spectral line, the following are obtained:

- I_i and ΔI_i : the peak intensity and its uncertainty,
- σ_i and $\Delta\sigma_i$: the Gaussian width (standard deviation) and its uncertainty,
- λ_i and $\Delta\lambda_i$: the line centroid and its uncertainty (not used in radiance calculations).

The total radiance \mathcal{I}_i of the line is computed as:

$$(9) \quad \mathcal{I}_i = \sqrt{2\pi} \cdot I_i \cdot \sigma_i.$$

Uncertainties on the radiance are propagated from the fitting parameters via standard first-order error propagation:

$$(10) \quad \frac{\Delta\mathcal{I}_i}{\mathcal{I}_i} = \sqrt{\left(\frac{\Delta I_i}{I_i}\right)^2 + \left(\frac{\Delta\sigma_i}{\sigma_i}\right)^2}.$$

These radiance uncertainties $\Delta\mathcal{I}_i$ are then used as input for the FIP bias uncertainty estimation that are going to be presented in Sec. C.2.

C.2. Error Estimation on FIP Bias Values Uncertainty in the FIP bias values, as defined in Eq. 3 and based on the combination ratio method ([Zambrana Prado & Buchlin, 2019](#)), is estimated using a first-order approximation. The relative error in the FIP bias \mathfrak{R} is given by:

$$(11) \quad \frac{\Delta\mathfrak{R}}{\mathfrak{R}} = \frac{\sum_{i \in (\text{LF})} \alpha_i \Delta\mathcal{I}_i / A_i^P}{\sum_{i \in (\text{LF})} \alpha_i \mathcal{I}_i / A_i^P} + \frac{\sum_{j \in (\text{HF})} \beta_j \Delta\mathcal{I}_j / A_j^P}{\sum_{j \in (\text{HF})} \beta_j \mathcal{I}_j / A_j^P},$$

where \mathcal{I}_i and $\Delta\mathcal{I}_i$ are the radiance and its uncertainty for line i , A_i^P are the photospheric abundances, and α_i and β_j are the coefficients used for the FIP bias calculation (Eq. 3).

D. Light Curve Computation Method

To extract reliable information on temporal variations from EUI/FSI₁₇₄ light curves, despite the absence of absolute radiometric calibration and of time-dependent flat-field correction in EUI data release 6.0, we developed a correction method that normalizes the intensity time series within selected regions of interest (ROIs). This approach compensates for fluctuations caused by spacecraft pointing changes, which shift the ROI across different detector areas with different responses. Our goal is not to retrieve absolute intensities, but to recover consistent, relative intensity variations over time that can be used to track plumes evolution.

- (1) For each observation, we compute the mean intensity within the ROI and extract the World Coordinate System (WCS) metadata: `CRVAL1` and `CRVAL2` (image center

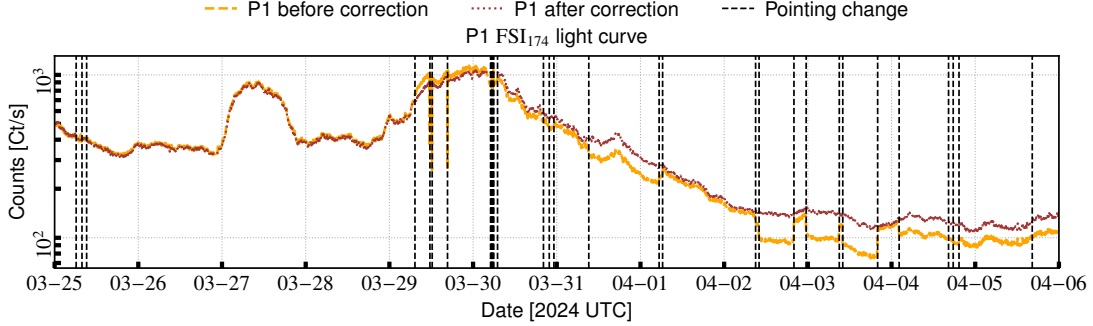


FIGURE 10. Example light curve from region “P1” in EU1/FSI₁₇₄. Orange: raw intensity. Red: corrected intensity after pointing jump normalization. Dashed vertical lines indicate detected pointing changes.

coordinates in arcseconds), and CDELTA1, CDELTA2 (pixel scale in arcsec/pixel along x and y).

- (2) We compute the pixel-scale pointing displacement between consecutive images as:

$$D_{px} = \sqrt{\left(\frac{\Delta\text{CRVAL1}}{\text{CDELTA1}}\right)^2 + \left(\frac{\Delta\text{CRVAL2}}{\text{CDELTA2}}\right)^2}$$

where $\Delta\text{CRVAL}i$ is the difference in image center coordinates between two consecutive observations. Thus, D_{px} is the effective pixel displacement between successive pointings. A jump is flagged if $D_{px} > 2$ pixels.

- (3) Temporal segments between two pointing changes that contain fewer than three measurements are discarded to ensure statistical robustness.
- (4) The mask is refined iteratively to remove all segments that are too short. Pointing displacements are recomputed using the filtered set until convergence is reached.
- (5) For each remaining pointing change at index n , we compute a correction factor based on the mean intensity before and after the jump using the first light curve (“P1” in our case):

$$(12) \quad f_{\text{adj}} = \frac{I_{\text{pre}}}{I_{\text{post}}} = \frac{\frac{1}{l} \sum_{k=n-l}^{n-1} I_k^{(0)}}{\frac{1}{l} \sum_{k=n}^{n+l-1} I_k^{(0)}}$$

where $I_k^{(0)}$ is the mean intensity of the first contour at time step k , and $l = 3$ is the averaging window length. This ensures stability in both pre- and post-jump estimates.

- (6) The factor f_{adj} is then applied to all subsequent intensities in all ROIs (e.g. “P1” and “P2”):

$$(13) \quad I_m^{(i)} \rightarrow \frac{I_m^{(i)}}{f_{\text{adj}}}, \quad \forall m \geq n, \forall i$$

Applying a common correction factor across ROIs is justified if the ROIs are located sufficiently close to each other (within ~ 500 pixels on the detector), and if large ROI sizes ensure local detector response variations are averaged out.

By applying this correction iteratively across all detected pointing jumps, we obtain smoothed and consistent light curves that more accurately reflect actual coronal variability. This correction is particularly important given the current calibration state of EU1/FSI₁₇₄.

Figure 10 shows the light curve from region “P1” before (orange) and after (red) correction. Black dashed lines indicate the time steps where a pointing jump was identified and corrected. Several of these discontinuities are significantly reduced by the correction.

References

- Alterman B. L., Rivera Y. J., Lepri S. T., Raines J. M., D'Amicis R., 2025, *A&A*, 700, A23
- Brooks D., 2015, in *AGU Fall Meeting Abstracts*. pp SH54B–06
- Brooks D. H., Warren H. P., 2011, *ApJ*, 727, L13
- Cao W., Gorceix N., Coulter R., Ahn K., Rimmele T. R., Goode P. R., 2010, *Astronomische Nachrichten*, 331, 636
- Chae J., Lee K.-S., 2023, *ApJ*, 954, 45
- Chae J., Cho K., Nakariakov V. M., Cho K.-S., Kwon R.-Y., 2021, *ApJ*, 914, L16
- Cho K.-S., et al., 2023, *ApJ*, 953, 69
- Culhane J. L., et al., 2007, *Sol. Phys.*, 243, 19
- DeForest C. E., Plunkett S. P., Andrews M. D., 2001, *ApJ*, 546, 569
- Del Zanna G., Bromage B. J. I., 1999, in Vial J. C., Kaldeich-Schü B., eds, *ESA Special Publication Vol. 446, 8th SOHO Workshop: Plasma Dynamics and Diagnostics in the Solar Transition Region and Corona*. p. 269
- Del Zanna G., Bromage B. J. I., Mason H. E., 2003, *A&A*, 398, 743
- Del Zanna G., Rozum I., Badnell N. R., 2008, *A&A*, 487, 1203
- Dere K. P., Landi E., Mason H. E., Monsignor Fossi B. C., Young P. R., 1997, *A&AS*, 125, 149
- Domingo V., Fleck B., Poland A. I., 1995, *Sol. Phys.*, 162, 1
- Doschek G. A., Laming J. M., Warren H. P., Lemaire P., Wilhelm K., 1997, in *AAS/Solar Physics Division Meeting #28*. p. 04.04
- Dufresne R. P., Del Zanna G., Young P. R., Dere K. P., Deliporanidou E., Barnes W. T., Landi E., 2024, *ApJ*, 974, 71
- Feldman U., Schühle U., Widing K. G., Laming J. M., 1998, *ApJ*, 505, 999
- Fu H., Madjarska M. S., Xia L., Li B., Huang Z., Wangguan Z., 2017, *ApJ*, 836, 169
- Geiss J., Gloeckler G., von Steiger R., 1995, *Space Sci. Rev.*, 72, 49
- Grevesse N., Asplund M., Sauval A. J., 2007, *Space Sci. Rev.*, 130, 105
- Guennou C., Hahn M., Savin D. W., 2015, *ApJ*, 807, 145
- Harris C. R., et al., 2020, *Nature*, 585, 357
- Harrison R. A., et al., 1995, *Sol. Phys.*, 162, 233
- Huang Z., et al., 2023, *A&A*, 673, A82
- Hunter J. D., 2007, *Computing in Science & Engineering*, 9, 90
- Jess D. B., Mathioudakis M., Erdélyi R., Crockett P. J., Keenan F. P., Christian D. J., 2009, *Science*, 323, 1582
- Jess D. B., Pascoe D. J., Christian D. J., Mathioudakis M., Keys P. H., Keenan F. P., 2012, *ApJ*, 744, L5
- Jordan C., Macpherson K. P., Smith G. R., 2001, *MNRAS*, 328, 1098
- Khomenko E., Cally P. S., 2012, *ApJ*, 746, 68
- Kosugi T., et al., 2007, *Sol. Phys.*, 243, 3
- Koukras A., Savin D. W., Hahn M., 2023, in *AGU Fall Meeting Abstracts*. pp SH43B–3144
- Kramida A., Yu. Ralchenko Reader J., and NIST ASD Team 2024, *NIST Atomic Spectra Database (ver. 5.12)*, [Online]. Available: <https://physics.nist.gov/asd> [2025, February 21]. National Institute of Standards and Technology, Gaithersburg, MD.
- Kumar P., Karpen J. T., Uritsky V. M., DeForest C. E., Raouafi N. E., Richard DeVore C., 2022, *ApJ*, 933, 21
- Laming J. M., 2009, *ApJ*, 695, 954
- Laming J. M., 2015, *Living Reviews in Solar Physics*, 12, 2

- Laming J. M., et al., 2019, *ApJ*, 879, 124
- Levenberg K., 1944, *Quarterly of applied mathematics*, 2, 164
- Marquardt D. W., 1963, *Journal of the society for Industrial and Applied Mathematics*, 11, 431
- Martin W. C., Wiese W. L., Kramida A., 2023, *Atomic Spectroscopy*. Springer International Publishing, Cham, pp 177–197, doi:10.1007/978-3-030-73893-8_11, https://doi.org/10.1007/978-3-030-73893-8_11
- Mason H. E., Bochsler P., 1999, *Space Sci. Rev.*, 87, 105
- McKerns M. M., Strand L., Sullivan T., Fang A., Aivazis M. A. G., 2012, *Building a Framework for Predictive Science* (arXiv:1202.1056), <https://arxiv.org/abs/1202.1056>
- Meyer J. P., 1985, *ApJS*, 57, 173
- Müller D., et al., 2020, *A&A*, 642, A1
- Murabito M., et al., 2024, *Phys. Rev. Lett.*, 132, 215201
- Panesar N. K., Sterling A. C., Moore R. L., Tiwari S. K., De Pontieu B., Norton A. A., 2018, *ApJ*, 868, L27
- Poletto G., 2015, *Living Reviews in Solar Physics*, 12, 7
- Pottasch S. R., 1963, *ApJ*, 137, 945
- Raouafi N. E., Stenborg G., 2014, *ApJ*, 787, 118
- Raouafi N. E., et al., 2023, *ApJ*, 945, 28
- Reames D. V., 2018, *Sol. Phys.*, 293, 47
- Rochus P., et al., 2020, *A&A*, 642, A8
- SPICE Consortium et al., 2020, *A&A*, 642, A14
- SPICE Consortium et al., 2024, *Data issued from SPICE instrument on Solar Orbiter: data release 5.0*, doi:10.48326/IDOC.MEDOC.SPICE.5.0, <https://spice.osups.universite-paris-saclay.fr/spice-data/release-5.0/release-notes.html>
- Saito K., 1965, *PASJ*, 17, 1
- Sheeley N. R., et al., 1997, *ApJ*, 484, 472
- Shimizu T., et al., 2020, in *Space Telescopes and Instrumentation 2020: Ultraviolet to Gamma Ray*. pp 113–119
- Sinjan J., et al., 2023, *Astronomy & Astrophysics*, 673, A31
- Solanki S. K., et al., 2020, *A&A*, 642, A11
- Srivastava A. K., et al., 2017, *Scientific Reports*, 7, 43147
- Stansby D., Baker D., Brooks D. H., Owen C. J., 2020, *A&A*, 640, A28
- Tritschler A., et al., 2015, in *18th Cambridge Workshop on Cool Stars, Stellar Systems, and the Sun*. pp 933–944
- Uritsky V. M., DeForest C. E., Karpen J. T., DeVore C. R., Kumar P., Raouafi N. E., Wyper P. F., 2021, *ApJ*, 907, 1
- Varesano T., et al., 2024, *A&A*, 685, A146
- Virtanen P., et al., 2020, *Nature Methods*, 17, 261
- Wang Y. M., Grappin R., Robbrecht E., Sheeley Jr. N. R., 2012, *ApJ*, 749, 182
- Watanabe T., 2014, in *Oschmann Jacobus M. J., Clampin M., Fazio G. G., MacEwen H. A., eds, Society of Photo-Optical Instrumentation Engineers (SPIE) Conference Series Vol. 9143, Space Telescopes and Instrumentation 2014: Optical, Infrared, and Millimeter Wave*. p. 91431O, doi:10.1117/12.2055366
- Weberg M., Warren H., Crump N., Barnes W., 2023, *The Journal of Open Source Software*, 8, 4914
- Wilhelm K., Bodmer R., 1998, *Space Sci. Rev.*, 85, 371

Wilhelm K., et al., 1995, Sol. Phys., 162, 189
Wilhelm K., et al., 2011, A&A Rev., 19, 35
Yardley S. L., et al., 2023, ApJS, 267, 11
Yardley S. L., et al., 2024, Nature Astronomy, 8, 953
Young P. R., 2018, ApJ, 855, 15
Young P. R., Klimchuk J. A., Mason H. E., 1999, A&A, 350, 286
Zambrana Prado N., Buchlin É., 2019, A&A, 632, A20
Zambrana Prado N., Kucera T. A., Young P., Buchlin E., Fazakerley A., Reid H., Pelouze G., 2025, MNRAS
van de Hulst H. C., 1950, Bull. Astron. Inst. Netherlands, 11, 150

UNIVERSITÉ PARIS-SACLAY, CNRS, INSTITUT D'ASTROPHYSIQUE SPATIALE, 91405 ORSAY, FRANCE
Email address: slimane.mzerguat@universite-paris-saclay.fr

ESTEC, EUROPEAN SPACE AGENCY, KEPLERLAAN 1, PO BOX 299, NL-2200 AG NOORDWIJK, THE NETHERLANDS

UNIVERSITÉ PARIS-SACLAY, CNRS, INSTITUT D'ASTROPHYSIQUE SPATIALE, 91405 ORSAY, FRANCE

MULLARD SPACE SCIENCE LABORATORY, UNIVERSITY COLLEGE LONDON, HOLMBURY ST MARY, DORKING, SURREY RH5 6NT, UK

ESTEC, EUROPEAN SPACE AGENCY, KEPLERLAAN 1, PO BOX 299, NL-2200 AG NOORDWIJK, THE NETHERLANDS

CENTRE FOR ASTROPHYSICS & RELATIVITY, SCHOOL OF PHYSICAL SCIENCES, DUBLIN CITY UNIVERSITY, DUBLIN D09 V209, IRELAND

ASTRONOMY & ASTROPHYSICS SECTION, DUBLIN INSTITUTE FOR ADVANCED STUDIES, DUBLIN D02 XF86, IRELAND

MULLARD SPACE SCIENCE LABORATORY, UNIVERSITY COLLEGE LONDON, HOLMBURY ST MARY, DORKING, SURREY RH5 6NT, UK

Email address: slimane.mzerguat@u-psud.fr